nature immunology

Commensal bacteria direct selective cargo sorting to promote symbiosis

Qin Zhang[1,4], Ying Pan[1,4], Ruiqing Yan[1], Benhua Zeng[2], Haifang Wang[1], Xinwen Zhang[1], Wenxia Li[2], Hong Wei[2] & Zhihua Liu[1,3]

Mucosal immunity protects a host from intestinal inflammation and infection and is profoundly influenced by symbiotic bacteria. Here we report that in mice symbiotic bacteria directed selective cargo sorting in Paneth cells to promote symbiosis through Nod2, a cytosolic bacterial sensor, and the multifunctional protein kinase LRRK2, both encoded by inflammatory bowel disease (IBD)-associated genes. Commensals recruited Nod2 onto lysozyme-containing dense core vesicles (DCVs), which was required for DCV localization of LRRK2 and a small GTPase, Rab2a. Deficiency of Nod2, LRRK2 or Rab2a or depletion of commensals resulted in lysosomal degradation of lysozyme. Thus, commensal bacteria and host factors orchestrate the lysozyme-sorting process to protect the host from enteric infection, implicating Paneth cell dysfunction in IBD pathogenesis.

© 2015 Nature America, Inc. All rights reserved.
chinaXiv:201605.01367v1
npg

Intestinal homeostasis depends on proper interactions between the mucosal immune system and intestinal microbiota. The complex nature of the symbiotic interactions between the host and microbes is beginning to be explored. Commensals can alter gene transcription, induce epigenetic modification and promote the differentiation of specific cell lineages[1–3]. However, many other possible mechanisms of symbiotic interactions remain to be explored.

Inflammatory bowel disease (IBD) is a clinical manifestation of disturbed intestinal homeostasis arising from the interaction between environmental and genetic factors. IBD includes two main forms: Crohn's disease and ulcerative colitis. Three major *NOD2* mutations have been associated with Crohn's disease[4,5]. *NOD2* encodes a cytosolic bacterial sensor that induces the expression of cytokines and antimicrobial peptide genes in response to the bacterial peptidoglycan muramyl dipeptide (MDP). *Nod2*$^{-/-}$ mice have been widely used to investigate the function of Nod2 in mucosal immunity and intestinal inflammation. *Nod2*$^{-/-}$ mice have an altered composition of commensal bacteria and increased susceptibility to enteric infection and piroxicam-induced ileitis[6–8]. However, the cellular and molecular mechanisms underlying the intestinal abnormalities in *Nod2*$^{-/-}$ mice remain to be further investigated. *LRRK2*, originally identified as the gene mutated in familial Parkinson's disease, was found to be a major susceptibility gene for IBD[9–13]. LRRK2 encodes a large cytosolic protein kinase whose function in mucosal immunity is not fully understood[14,15].

Paneth cells, a group of secretory cells located at the bottom of small intestinal crypts, have a vital role in maintaining the function of the epithelial barrier by secreting a range of antimicrobial peptides (AMPs) into the intestinal lumen. The AMPs secreted by Paneth cells include cryptdin, Reg3γ, lysozyme and others[16]. Depleting Paneth cells in mice results in a compromised intestinal barrier and enhanced translocation and dissemination of pathogens[17]. Several IBD-associated genes affect the function of Paneth cells[6,18–24], which suggests that dysfunctional Paneth cells might underlie the pathogenesis of IBD. Currently, many important cellular processes in Paneth cells, such as intracellular trafficking of AMPs, are not fully understood.

Within Paneth cells, the various AMPs are sorted after synthesis into specialized secretory granules called dense core vesicles (DCVs). Not much is known about the mechanisms by which cargos are selectively sorted and transported into DCVs after they exit the trans-Golgi network. A sorting-by-retention mechanism has been suggested by a study in *C. elegans* showing that loss of Rab2a function leads to specific lysosomal degradation of a neuropeptide[25]. Whether such a mechanism exists in mammalian cells remains unknown.

Here we investigated the function of LRRK2 in mucosal immunity, which led us to the discovery that symbiotic bacteria direct a DCV cargo-sorting process to promote symbiosis. We found high expression of LRRK2 in Paneth cells, and LRRK2 deficiency caused a specific deprivation of lysozyme in Paneth cells, which rendered *Lrrk2*$^{-/-}$ mice more susceptible to intestinal but not systemic *Listeria monocytogenes* infection. The lysozyme defect in *Lrrk2*$^{-/-}$ Paneth cells was due to failed recruitment of Rab2a onto the DCV surface. In addition, the presence of luminal biota was required for DCV sorting of lysozyme. In germ-free (GF) mice lysozyme was targeted for lysosomal degradation rather than secretion in Paneth cells. Finally, we determined that Nod2 was responsible for sensing commensal bacteria to direct lysozyme sorting in Paneth cells. Collectively, our data demonstrate that commensal bacteria direct lysozyme sorting

[1]Key Laboratory of Infection and Immunity of CAS, Institute of Biophysics, Chinese Academy of Sciences, Beijing, China. [2]Department of Laboratory Animal Science, College of Basic Medical Sciences, Third Military Medical University, Chongqing, China. [3]CAS Center for Excellence in Biomacromolecules, Chinese Academy of Sciences, Beijing, China. [4]These authors contributed equally to this work. Correspondence should be addressed to Z.L. (zhihualiu@ibp.ac.cn) or H. Wei (weihong63528@163.com).

Received 19 February; accepted 29 June; published online 3 August 2015; doi:10.1038/ni.3233

in Paneth cells through a Nod2-LRRK2-Rab2a axis, which in turn is important in controlling intestinal infection.

RESULTS

Enhanced susceptibility of *Lrrk2*$^{-/-}$ mice to intestinal infection

To determine the physiological function of LRRK2, we carried out immunofluorescence staining of mouse ileal sections. We noted high expression of LRRK2 in lysozyme-positive Paneth cells (**Fig. 1a**,**b**), as well as in myeloid cells in the lamina propria (data not shown), as previously reported[15]. We confirmed the specificity of LRRK2 immunostaining by simultaneously immunostaining ileal sections from *Lrrk2*$^{-/-}$ mice as controls (**Supplementary Fig. 1a**). Immunoblotting analysis also indicated the expression of LRRK2 in sorted CD24^{+} Paneth cells (**Supplementary Fig. 1b**,**c**). LRRK2 was concentrated on the surface of DCVs, as identified by lysozyme staining or granule structures in differential interference contrast images (**Fig. 1b**). To determine whether LRRK2 was required for the bactericidal function of Paneth cells, we orally infected wild-type and *Lrrk2*$^{-/-}$ mice with the Gram-positive intracellular bacterium *L. monocytogenes*, as the bactericidal activity of Paneth cells is required for effective clearance of this pathogen[6,20]. Bacterial loads were significantly increased in fecal samples and liver from infected *Lrrk2*$^{-/-}$ mice compared with those from wild-type mice (**Fig. 1c**). We noticed a similar trend in the spleen, but the difference was not significant (**Fig. 1c**). We observed no difference between wild-type and *Lrrk2*$^{-/-}$ mice in the number of bacteria recovered from liver and spleen 24 or 48 h after infection by intravenous injection of *L. monocytogenes* (**Supplementary Fig. 1d**), which indicated that LRRK2 deficiency leads to a specific defect in controlling intestinal infection.

Because Paneth cells can modulate intestinal microbiota, we investigated whether changes in intestinal flora in *Lrrk2*$^{-/-}$ mice could influence their susceptibility to intestinal *L. monocytogenes* infection[16]. We deep sequenced 16s rRNA genes of intestinal microbes from wild-type and *Lrrk2*$^{-/-}$ mice. Taxonomy-based analysis did not show any broad alterations in the phylum or family composition of bacterial commensals in *Lrrk2*$^{-/-}$ mice compared with that in wild-type mice (**Supplementary Fig. 1e**,**f**). However, some changes were observed for several minor families (**Supplementary Table 1**). For example, the relative abundance of *Erysipelotrichaceae* in the Firmicute phylum was higher in *Lrrk2*$^{-/-}$ mice than in wild-type mice (0.58% in wild-type mice versus 3.1% in *Lrrk2*$^{-/-}$ mice, $P < 0.01$). Principal-component analysis showed differential clustering patterns of intestinal microbiota communities between wild-type and *Lrrk2*$^{-/-}$ mice (**Supplementary Fig. 1g**). These results indicate that LRRK2 deficiency leads to alternations in microbial composition. However, further investigations that carefully consider the effects of the housing facility, caging and maternal transmission on the variation of microbial communities are required for more conclusive conclusions regarding the effect of *Lrrk2* deletion on microbiota composition. For the purpose of this study, to determine whether the altered microbiota in the *Lrrk2*$^{-/-}$ mice affected their susceptibility to *L. monocytogenes* infection, we transferred stool samples from wild-type and *Lrrk2*$^{-/-}$ mice to GF mice and orally infected the recipient mice with *L. monocytogenes* 2 weeks later. We did not observe significant differences in the *L. monocytogenes* burden between the two groups of recipient mice (**Fig. 1d**), which indicated that the alterations in the intestinal flora in *Lrrk2*$^{-/-}$ mice did not affect their susceptibility to intestinal *Listeria* infection. These results suggest that LRRK2 deficiency leads to a defect in the control of intestinal infection and that this defect is independent of altered microbiota in *Lrrk2*$^{-/-}$ mice.

LRRK2 deficiency leads to lysozyme deficiency in Paneth cells

We asked how LRRK2 deficiency might affect the bactericidal activity of Paneth cells. Periodic acid–Schiff staining did not reveal any apparent morphological difference between Paneth cells from wild-type and *Lrrk2*$^{-/-}$ mice (**Supplementary Fig. 2a**). However, electron microscopy analysis showed an increased percentage of DCVs with enlarged halo regions in *Lrrk2*$^{-/-}$ Paneth cells compared with wild-type

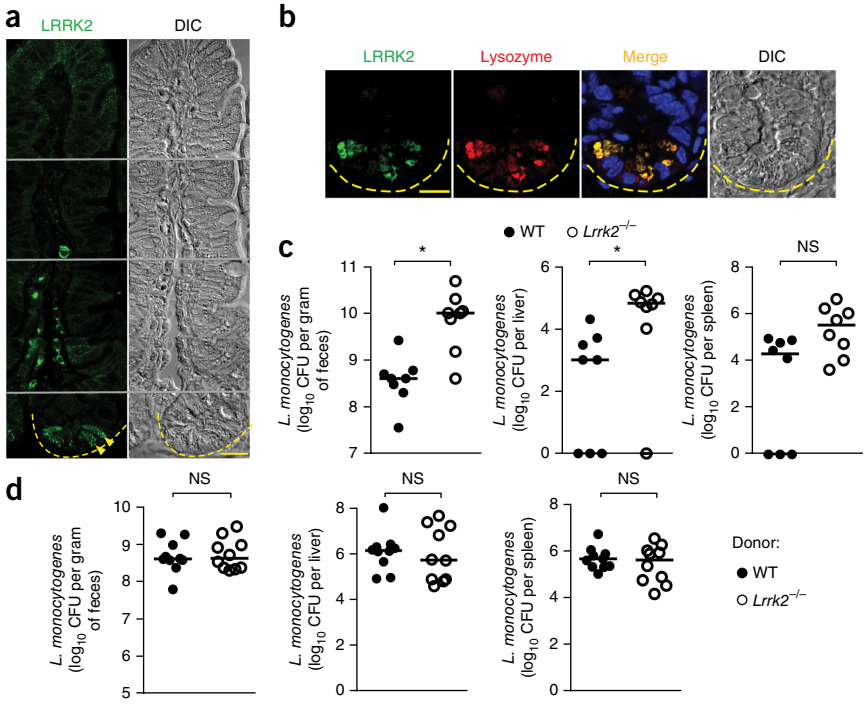

Figure 1 *Lrrk2*$^{-/-}$ mice are more susceptible to *Listeria* infection. (**a**) Confocal images of wild-type ileal sections immunostained with anti-LRRK2. Multiple images were aligned to show a complete villus (points of alignment are indicated by horizontal gray lines). Dashed yellow lines indicate the base of the crypt. Yellow arrowheads mark LRRK2^{+} cells at the bottom of the crypt. Scale bar, 20 µm. (**b**) Confocal images of a crypt from wild-type ileum immunostained for LRRK2 and lysozyme. Nuclei were counterstained with Hoescht 33342 (blue). Dashed yellow lines indicate the base of the crypt. Scale bar, 10 µm. (**c**) Numbers of bacteria (colony-forming units (CFU)) present in feces 10 h after infection and in livers and spleens 72 h after infection in wild-type ($n = 8$) and *Lrrk2*$^{-/-}$ ($n = 8$) mice infected with 10^9 CFU of *L. monocytogenes* by oral gavage. (**d**) Numbers of bacteria (CFU) present in feces 10 h after infection and in livers and spleens 72 h after infection in GF wild-type mice that received microbiota from the indicated donor mice ($n = 10$ for each group) and were then infected with 10^9 CFU of *L. monocytogenes* by oral gavage. In **c** and **d**, each symbol represents an individual animal, and horizontal bars indicate median values. WT, wild type; DIC, differential interference contrast. Data are representative of three (**a**–**c**) or two (**d**) independent experiments. *$P < 0.01$; NS, not significant ($P > 0.05$) (Mann-Whitney test).

© 2015 Nature America, Inc. All rights reserved.

Paneth cells, which suggested defects during DCV maturation (**Supplementary Fig. 2b**,**c**). We investigated whether the composition of AMPs was altered in *Lrrk2*$^{-/-}$ Paneth cells. Immunostaining showed an almost complete absence of lysozyme in *Lrrk2*$^{-/-}$ Paneth cells (**Fig. 2a**,**b**). Of note, in DCVs localized away from the apical side of Paneth cells, referred to here as subapical DCVs, lysozyme staining was similar in *Lrrk2*$^{-/-}$ and wild-type Paneth cells (**Fig. 2a**). The expression of other AMPs in DCVs such as precursors of cryptdin (procryptdin) and Reg3γ was similar in *Lrrk2*$^{-/-}$ and wild-type Paneth cells (**Fig. 2c** and **Supplementary Fig. 2d**), which suggested that the lack of lysozyme in *Lrrk2*$^{-/-}$ Paneth cells was not due to a general defect in DCV formation. Paneth cells secrete DCV-derived AMPs when exposed to bacterial antigens or bacteria *in vitro*[26]. Supernatants and cell lysates from isolated crypts from *Lrrk2*$^{-/-}$ mice were devoid of lysozyme (**Fig. 2d**) and showed significantly decreased bactericidal activity against *L. monocytogenes* (**Fig. 2e**) compared with those from wild-type mice. Lectin–*Helix pomatia* agglutinin (HPA) staining of whole mounts of ileum showed colocalization of lysozyme with mucus in the intestinal lumens of wild-type mice; however, there was a lack of lysozyme staining in the mucus of *Lrrk2*$^{-/-}$ mice (**Fig. 2f**). In contrast, procryptdin staining in the intestinal lumen was similar between wild-type and *Lrrk2*$^{-/-}$ mice (**Supplementary Fig. 2e**), indicating normal DCV exocytosis in *Lrrk2*$^{-/-}$ Paneth cells. Thus, *Lrrk2* deficiency leads to a specific impairment in the expression of lysozyme, but not of other cargos such as procryptdin, in Paneth cells.

To determine whether decreased lysozyme secretion was responsible for the impaired clearance of intestinal *L. monocytogenes* in *Lrrk2*$^{-/-}$ mice, we supplemented wild-type and *Lrrk2*$^{-/-}$ mice with recombinant lysozyme or PBS (vehicle) by oral gavage for a week before orally infecting them with *L. monocytogenes* (**Supplementary Fig. 2f**). Lysozyme supplementation markedly reduced the bacterial burden of *L. monocytogenes* in feces and liver in *Lrrk2*$^{-/-}$ mice compared with vehicle-treated *Lrrk2*$^{-/-}$ mice (**Fig. 2g**), but it had no effect on wild-type mice (**Fig. 2g**). These results suggest that *Lrrk2*$^{-/-}$ mice have deficient lysozyme expression in Paneth cells and that this is the major cause of their increased susceptibility to intestinal *L. monocytogenes* infection.

Lysozyme in *Lrrk2*$^{-/-}$ Paneth cells is degraded in lysosomes

To uncover the molecular mechanism underlying lysozyme deficiency in *Lrrk2*$^{-/-}$ Paneth cells, we cultured crypt organoids, which contain authentic Paneth cells[27], from mouse ileal sections. Unlike wild-type Paneth cells (**Supplementary Fig. 3a**), cultured *Lrrk2*$^{-/-}$ Paneth cells did not contain detectable lysozyme protein (**Fig. 3a**), whereas lysozyme mRNA expression was comparable between isolated wild-type and *Lrrk2*$^{-/-}$ crypts (**Fig. 3b**). These data suggest that the lack of lysozyme in *Lrrk2*$^{-/-}$ Paneth cells is due to a post-transcriptional defect. Treatment with leupeptin, a lysosomal inhibitor, or Brefeldin A, an inhibitor of protein transport from the endoplasmic reticulum to the Golgi apparatus, effectively restored lysozyme protein in cultured *Lrrk2*$^{-/-}$ Paneth cells as determined by immunostaining and immunoblotting (**Fig. 3a**,**c** and **Supplementary Fig. 3b**). In contrast, knockdown of Rab27a, a small GTPase essential for DCV exocytosis, by transfection of the cultured organoids

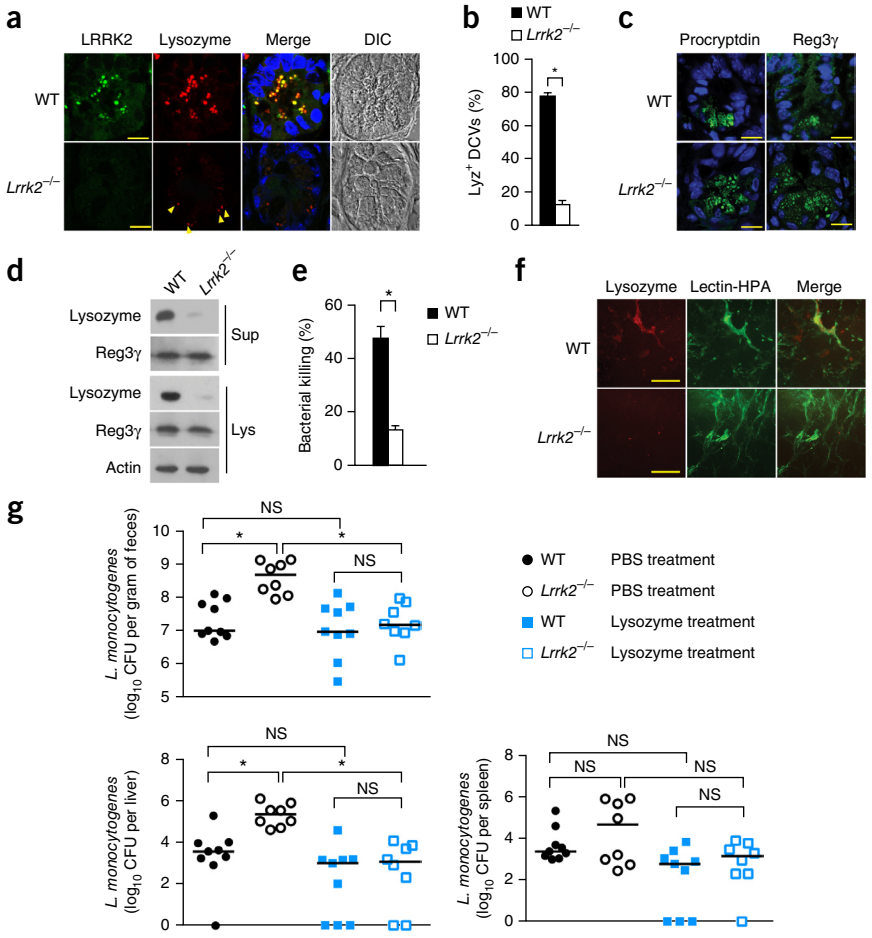

Figure 2 *Lrrk2*$^{-/-}$ Paneth cells are lysozyme deficient. (**a**) Confocal images of crypts from wild-type and *Lrrk2*$^{-/-}$ mice showing LRRK2 and lysozyme. Blue, counterstained nuclei. Arrowheads mark subapical DCVs. Scale bars, 10 μm. (**b**) Percentage of lysozyme-positive (Lyz^{+}) DCVs in Paneth cells as shown in **a**. DCVs from 30 Paneth cells per mouse were quantified in three mice of each genotype. Data are expressed as mean and s.e.m. $^{*}P < 0.01$, Student's *t*-test. (**c**) Confocal images of procryptdin and Reg3γ in wild-type and *Lrrk2*$^{-/-}$ mice. Blue, counterstained nuclei. Scale bars, 10 μm. (**d**) Immunoblots for lysozyme in supernatant (Sup) and lysate (Lys) fractions from isolated small intestinal crypts stimulated with 1 μg ml^{-1} LPS for 30 min. Reg3γ and actin were used as loading controls for the Sup and Lys fractions, respectively. (**e**) Bactericidal activity against *L. monocytogenes* in supernatants from **d**. Data are expressed as the percentage of bacteria killed compared with amounts in unstimulated crypts (mean of triplicates + s.e.m.). $^{*}P < 0.01$ (Student's *t*-test). (**f**) Whole-mount images of tissues from wild-type and *Lrrk2*$^{-/-}$ mice taken from immediately above the ileal mucosal surface and stained with lectin-HPA and a lysozyme antibody. Scale bars, 20 μm. (**g**) Numbers of bacteria in feces 10 h after infection and in livers and spleens 72 h after infection in mice infected as described in **Figure 1d**. $n = 9$ for wild-type treatment groups; $n = 8$ for *Lrrk2*$^{-/-}$ treatment groups. $^{*}P < 0.01$; NS, $P > 0.05$ (Mann-Whitney tests). Each symbol represents an individual animal; horizontal bars indicate median values. Data are representative of three (**a**–**f**) or two (**g**) independent experiments.

© 2015 Nature America, Inc. All rights reserved.

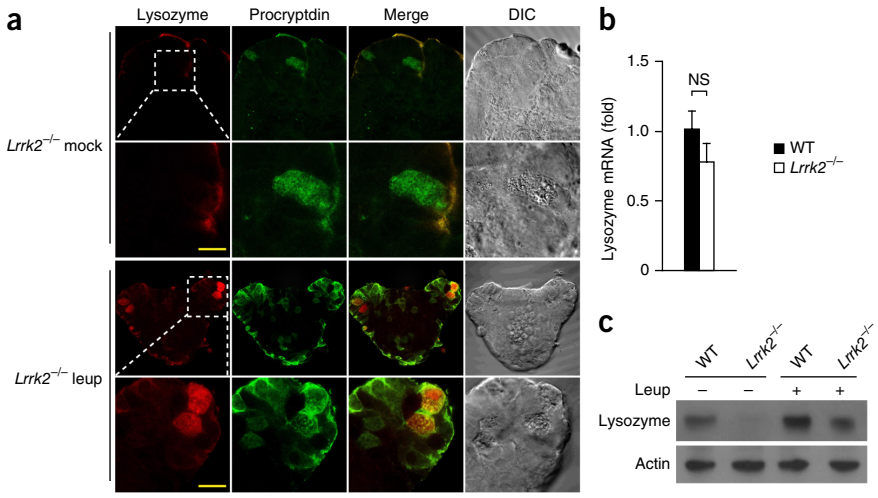

Figure 3 Lysozyme is degraded in *Lrrk2*$^{-/-}$ Paneth cells. (**a**) Confocal images of lysozyme and procryptdin in cultured *Lrrk2*$^{-/-}$ crypt organoids treated with 100 μM leupeptin (leup) or mock treated for 24 h. Boxed areas are shown at higher magnification in the panels below. Scale bars, 10 μm. (**b**) Quantitative RT-PCR analysis of mRNA encoding lysozyme among all mRNA in isolated wild-type and *Lrrk2*$^{-/-}$ crypts. mRNA results were calculated as the change in threshold cycle number ($2^{-\Delta Ct}$) relative to that of the control gene *Gapdh*. Data are expressed as the mean for three individual animals + s.e.m. NS, $P > 0.05$ (Student's *t*-test). (**c**) Immunoblot of lysozyme in wild-type and *Lrrk2*$^{-/-}$ organoids treated as in **a**. Actin was used as a loading control. Data in all panels are representative of three independent experiments.

with a Rab27a-specific short interfering RNA (siRNA) oligo failed to restore lysozyme in *Lrrk2*$^{-/-}$ Paneth cells compared with expression in organoids transfected with control siRNA, as determined by immunostaining (**Supplementary Fig. 3c**). These data collectively indicate that *Lrrk2* deficiency leads to the degradation of lysozyme in lysosomes.

LRRK2 recruits Rab2a onto DCVs for lysozyme sorting

DCV cargo sorting begins in the trans-Golgi network and persists throughout DCV maturation, during which factors not destined for DCVs are directed to the endosomal-lysosomal route[28,29]. During maturation, DCVs in Paneth cells are transported toward the apical side. On the basis of our observation that lysosome inhibition restored lysozyme in *Lrrk2*$^{-/-}$ Paneth cells, we tested whether LRRK2 deficiency altered the intracellular trafficking of DCV cargos. We employed yeast two-hybrid screening to identify LRRK2-interaction partners potentially implicated in DCV biogenesis and maturation (**Supplementary Table 2**). Two DCV-localized GTPases, Rab2a and Rab10, interacted with LRRK2 (**Fig. 4a**). Rab2a is required for DCV cargo sorting in *C. elegans*,

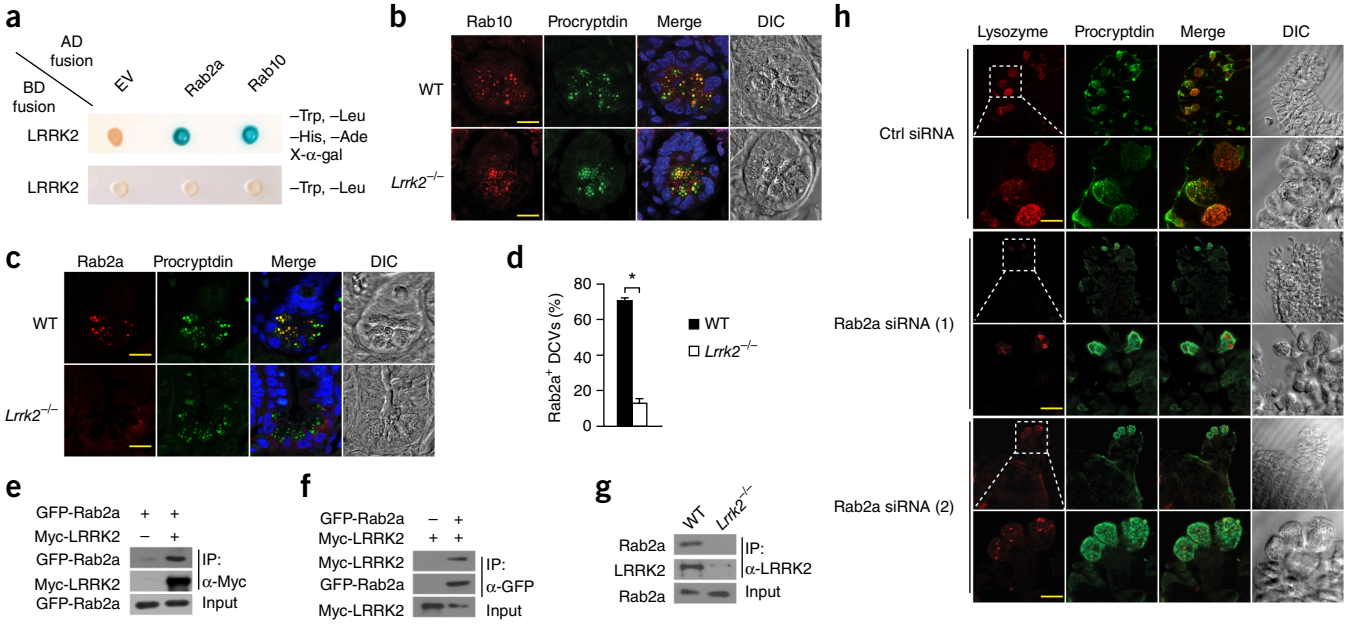

Figure 4 LRRK2 controls lysozyme sorting in DCVs by recruiting Rab2a. (**a**) Yeast two-hybrid assays of LRRK2 fused to the DNA-binding domain (BD) of the yeast transcriptional activator Gal4 and of Rab2a or Rab10 fused to the Gal4 activating domain (AD), assessed in plates with synthetic defined medium lacking (–) tryptophan (Trp), leucine (Leu), histidine (His) and adenine (Ade) as indicated, in the presence (top) or absence (bottom) of X-α-galactosidase (X-α-gal). EV, empty vector. (**b**,**c**) Confocal images of procryptdin, Rab10 (**b**) and Rab2a (**c**) in ileal crypts from wild-type and *Lrrk2*$^{-/-}$ mice. Blue, counterstained nuclei. Scale bars, 10 μm. (**d**) Percentage of Rab2a$^+$ DCVs as shown in **c**. DCVs from 30 Paneth cells per mouse were quantified for three mice of each genotype. Data are expressed as mean and s.e.m. $^*P < 0.01$ (Student's *t*-test). (**e**,**f**) Coimmunoprecipitation analysis of the interaction between overexpressed LRRK2 and Rab2a. Tagged proteins were overexpressed in HEK293T cells, immunoprecipitated (IP) with anti-Myc (**e**) or anti-GFP (**f**) beads and immunoblotted. (**g**) Coimmunoprecipitation analysis of the interactions between endogenous LRRK2 and Rab2a. LRRK2 and Rab2a were immunoblotted in crypt lysates (input) and after immunoprecipitation with anti-LRRK2. (**h**) Confocal images of lysozyme and procryptdin in cultured wild-type crypt organoids transfected with Rab2a-specific or control (Ctrl) siRNA oligos. Boxed areas are shown at higher magnification in the panels immediately below. Scale bars, 10 μm. Data are representative of three independent experiments.

© 2015 Nature America, Inc. All rights reserved.

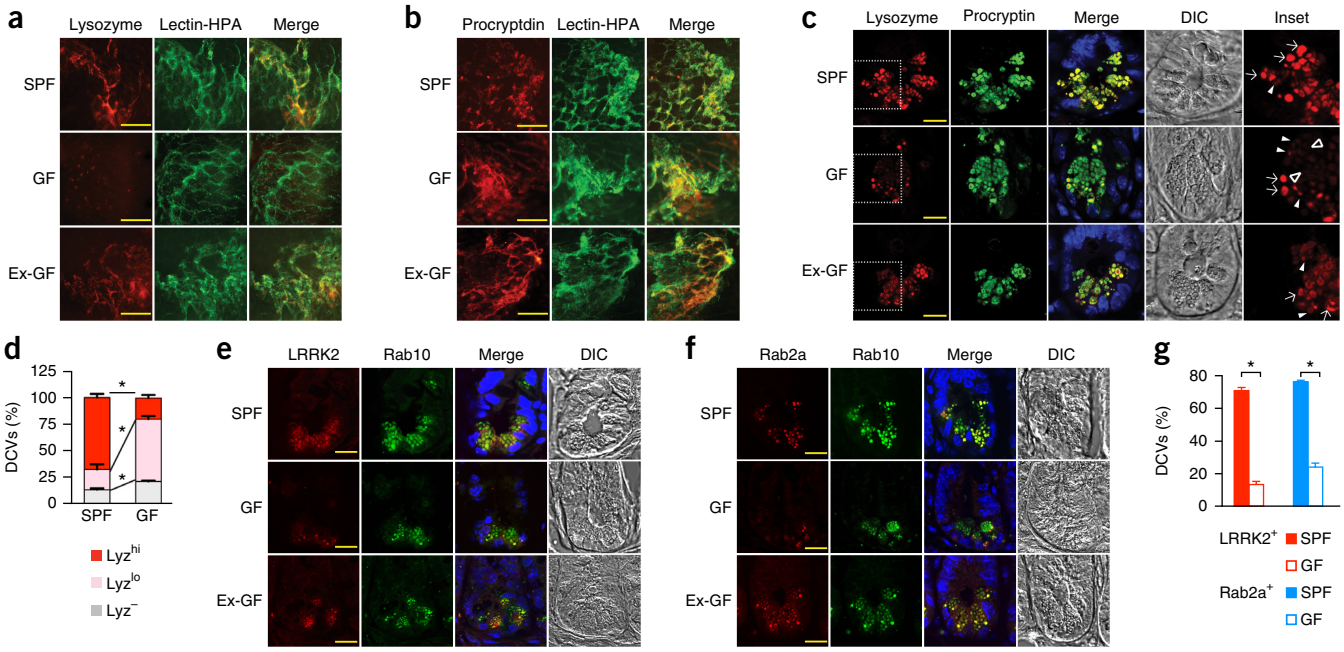

Figure 5 Commensal bacteria regulate lysozyme sorting. (**a**,**b**) Whole-mount images of tissues taken from immediately above the ileal mucosal surface in SPF, GF and conventionalized GF (ex-GF) mice and stained with lectin-HPA and anti-lysozyme (**a**) or anti-procryptdin (**b**). Scale bars, 20 μm. (**c**) Confocal images of the indicated proteins in SPF, GF and ex-GF ileal sections. Inset images (far right) are magnified views of the boxed areas in far left panels in the corresponding rows. DCVs were divided into three categories on the basis of fluorescence intensity as measured by ImageJ: hi, lo and absent (–). Arrows indicate Lyz^{hi} DCVs (signal ≥ 150); filled arrowheads indicate Lyz^{lo} DCVs (60 < signal < 150); open arrowheads indicate Lyz^{-} DCVs (signal < 60). Blue, counterstained nuclei. Scale bars, 10 μm. (**d**) Percentage of DCVs in each category as described in **c**. DCVs from 30 Paneth cells per mouse were quantified for three mice for each condition. Data are expressed as mean and s.e.m. (**e**,**f**) Confocal images of the indicated proteins in SPF, GF and ex-GF ileal sections. Blue, counterstained nuclei. Scale bars, 10 μm. (**g**) Percentage of $LRRK2^{+}$ and $Rab2a^{+}$ DCVs as shown in **e** and **f**. DCVs in 90 Paneth cells from three mice (30 from each mouse) were counted for each condition. Data are expressed as mean and s.e.m. $^{*}P < 0.01$ (Student's *t*-test). Data are representative of three independent experiments.

and loss of Rab2a results in lysosomal degradation of a mis-sorted neuropeptide[25,30]. *C. elegans* Rab10 mutants have severely defective DCV secretion[31]. We stained procryptdin to visualize DCVs in both wild-type and *Lrrk2*$^{-/-}$ Paneth cells (**Fig. 4b**,**c**). Rab10 localization was similar in wild-type and *Lrrk2*$^{-/-}$ Paneth cells (**Fig. 4b**). In contrast, Rab2a was largely undetectable in DCVs in *Lrrk2*$^{-/-}$ Paneth cells, except for a few subapical DCVs (**Fig. 4c**,**d**), whereas Rab2a was localized to DCVs in wild-type Paneth cells (**Fig. 4c**,**d**). Coimmunoprecipitation revealed interaction between LRRK2 and Rab2a when the proteins were overexpressed in HEK293T cells and between the endogenous proteins in isolated crypts (**Fig. 4e–g**). These observations suggest that LRRK2 might physically recruit Rab2a onto the DCV surface.

To determine whether Rab2a is required for lysozyme sorting in Paneth cells, we transfected cultured organoids with two different Rab2a-specific siRNA oligos or control siRNA. Transfection with Rab2a-specific oligos effectively reduced the amounts of Rab2a in cultured organoids relative to the amounts observed after transfection with control siRNA (**Supplementary Fig. 3d**). Rab2a knockdown did not affect amounts of LRRK2 (**Supplementary Fig. 3d**), but it led to the disappearance of lysozyme in Rab2a-specific siRNA–transfected Paneth cells compared with Paneth cells transfected with control siRNA (**Fig. 4h**). Furthermore, lysozyme in Paneth cells transfected with Rab2a siRNA was restored by lysosomal inhibition with leupeptin treatment as determined by immunostaining (**Supplementary Fig. 3e**). These results suggest that Rab2a deficiency leads to lysosomal degradation of lysozyme. Thus, our data support a role of the LRRK2-Rab2a axis in controlling specific cargo sorting in DCVs.

Commensal bacteria are required for lysozyme sorting in GF mice

We next asked whether commensal bacteria might regulate the lysozyme-sorting process. Whole-mount staining showed an absence of lysozyme in the intestinal lumens of GF mice, whereas the expression of procryptdin was similar between GF and specific-pathogen-free (SPF) mice (**Fig. 5a**,**b**). However, amounts of lysozyme mRNA and protein detected by quantitative PCR and immunohistochemical staining of ileal sections were similar between GF and SPF mice (**Supplementary Fig. 4a**,**b**), consistent with previous reports[32,33]. We next used immunofluorescence staining to analyze the distribution of lysozyme in Paneth cells in more detail. In ileal sections from GF mice, DCVs in Paneth cells showed a heterogeneous lysozyme-staining pattern, with apical DCVs having diminished lysozyme staining, compared with DCVs in Paneth cells from SPF mice (**Fig. 5c**,**d** and **Supplementary Fig. 4c**). In contrast to the heterogeneity of lysozyme staining in DCVs in GF mice, immunostaining revealed that procryptdin was more homogeneously distributed among DCVs throughout Paneth cells in GF mice (**Fig. 5c**). The protein amount of lysozyme was greatly reduced in crypts isolated from GF mice compared with crypts from SPF mice (**Supplementary Fig. 4d**). Inhibiting lysosomes with leupeptin restored the protein amounts of lysozyme in crypt organoids derived from GF mice as determined by immunostaining and immunoblotting (**Supplementary Fig. 4e**,**f**), which suggests that lysozyme is degraded in lysosomes in Paneth cells in GF mice. Because these observations were similar to the degradation of lysozyme in lysosomes in the *Lrrk2*$^{-/-}$ Paneth cells, we examined the cellular localization of LRRK2, Rab2a and Rab10 in Paneth cells from GF mice. LRRK2 and Rab2a proteins were almost completely

© 2015 Nature America, Inc. All rights reserved.

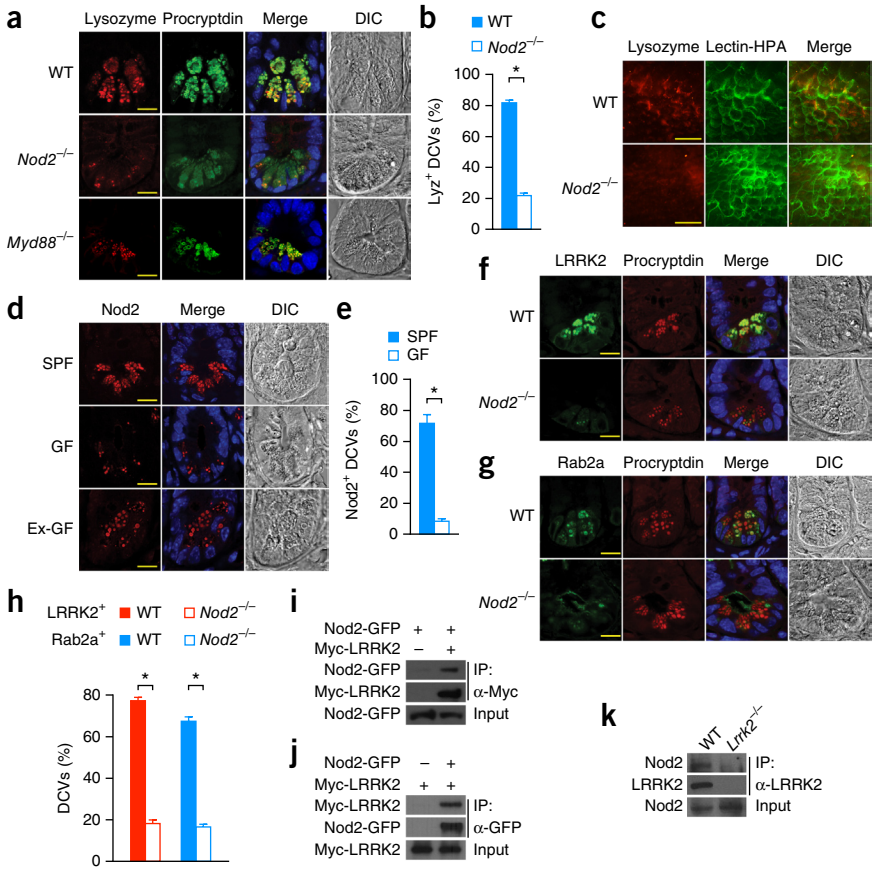

Figure 6 Nod2 mediates bacterially directed lysozyme sorting. (**a**) Confocal images of lysozyme and procryptdin in ileal sections from mice with the indicated genotypes. Blue, counterstained nuclei. Scale bars, 10 μm. (**b**) Percentage of lysozyme-positive DCVs in wild-type and *Nod2*$^{-/-}$ Paneth cells as shown in **a**. Quantification was done as described for **Figure 2b** for two mice of each genotype. Data are expressed as mean and s.e.m. (**c**) Whole-mount images of the ileal mucosal surface in the indicated mice as described in **Figure 2f**. Scale bars, 20 μm. (**d**,**f**,**g**) Confocal images of (**d**) Nod2, (**f**) LRRK2, (**g**) Rab2a and procryptdin in ileal sections from mice with the indicated genotypes. Blue, counterstained nuclei. Scale bars, 10 μm. (**e**,**h**) Percentage of Nod2$^+$ (**e**) and LRRK2$^+$ or Rab2a$^+$ (**h**) DCVs in Paneth cells from the indicated mice. Quantification was done as described in **Figure 2b** for three mice per condition (**e**) and two mice per genotype (**h**). Data are expressed as mean and s.e.m. (**i**,**j**) Coimmunoprecipitation analysis of the interaction between overexpressed Nod2 and LRRK2. Tagged proteins were expressed in HEK293T cells, immunoprecipitated with anti-Myc (**i**) or anti-GFP (**j**) beads and immunoblotted. (**k**) Coimmunoprecipitation analysis of the interaction between endogenous Nod2 and LRRK2. LRRK2 and Nod2 were immunoblotted in crypt lysates (input) and after immunoprecipitation with anti-LRRK2. $^*P < 0.01$ (Student's *t*-test). Data are representative of three independent experiments.

absent from more mature, apical DCVs in Paneth cells in GF mice compared with those in SPF mice (**Fig. 5e–g** and **Supplementary Fig. 5a**,**b**). However, quantitative RT-PCR analysis of mRNA and immunoblotting analysis of protein showed that amounts of LRRK2 and Rab2a mRNA and protein were not reduced in isolated crypts from GF mice compared with crypts from SPF mice (**Supplementary Fig. 5c**,**d**), which suggested that the loss of lysozyme in GF mice was due not to the loss of expression of LRRK2 and Rab2a but to the lack of DCV localization of LRRK2 and Rab2a. Furthermore, immunostaining and whole-mount staining showed that lysozyme sorting and secretion were restored in conventionalized GF mice compared with GF mice (**Fig. 5a**,**c**), which suggested that the presence of symbiotic bacteria was required to direct lysozyme sorting during DCV maturation. In addition, conventionalization of GF mice restored the cellular localization of lysozyme, LRRK2 and Rab2a in Paneth cells compared with that in GF mice (**Fig. 5e**,**f**), which indicated that the presence of commensals is required for lysozyme sorting.

Nod2 senses commensal bacteria to direct lysozyme sorting

Plasma membrane–bound Toll-like receptors (TLRs) and the cytoplasmic receptor Nod2 have been reported to sense bacterial products in Paneth cells[6,17]. To determine which of these is responsible for commensal-directed lysozyme sorting, we examined lysozyme distribution in Paneth cells from *Myd88*$^{-/-}$ mice (*Myd88* encodes a downstream adaptor of TLRs) and *Nod2*$^{-/-}$ mice. Approximately 78% of DCVs in *Nod2*$^{-/-}$ Paneth cells were devoid of lysozyme, compared with approximately 18% in wild-type Paneth cells (**Fig. 6a**,**b**), whereas the lysozyme distribution was normal in *Myd88*$^{-/-}$ Paneth cells (**Fig. 6a**). Because the loss of lysozyme in Paneth cell DCVs in *Nod2*$^{-/-}$ mice might have been influenced by genetic background and intestinal microbiota composition[34], we used siRNA to silence Nod2 in cultured organoids. Immunostaining showed a marked decrease in amounts of lysozyme protein in cultured organoids transfected with a Nod2-specific siRNA oligo compared with organoids transfected with control siRNA (**Supplementary Fig. 6a**,**b**). Previous studies using colorimetric immunohistochemistry (IHC) showed normal lysozyme staining in *Nod2*$^{-/-}$ Paneth cells[34]. We also found similar lysozyme staining between wild-type and *Nod2*$^{-/-}$ Paneth cells by colorimetric IHC (**Supplementary Fig. 6c**). We suggest that because of the nature of the colorimetric reactions, chromogen-based IHC is not suitable for studying a gradual cellular process such as cargo sorting. Whole-mount staining showed deficient lysozyme expression in the intestinal lumens of *Nod2*$^{-/-}$ mice compared with wild-type mice (**Fig. 6c**). *Nod2*$^{-/-}$ mice were more susceptible to intestinal *Listeria* infection even after being housed with wild-type mice for 2 weeks (**Supplementary Fig. 6d**), which indicated an effect independent of intestinal microbiota. Furthermore, immunostaining showed that lysosome inhibition by leupeptin treatment restored lysozyme in cultured *Nod2*$^{-/-}$ Paneth cells compared with amounts in mock-treated cells (**Supplementary Fig. 6e**,**f**). Thus, Nod2 is required for the sorting of lysozyme into DCVs, and *Nod2* deficiency leads to lysosomal degradation of lysozyme.

In SPF wild-type mice, Nod2 was localized on the surface of DCVs (**Fig. 6d**,**e** and **Supplementary Fig. 6g**,**h**), consistent with a previous study of human Paneth cells[35]. Immunoblotting also detected the expression of Nod2 in sorted CD24$^+$ Paneth cells (**Supplementary Fig. 6i**). Nod2 could not be detected on the surface of DCVs in GF mice (**Fig. 6d**,**e**), but its localization was restored in conventionalized GF mice (**Fig. 6d**), which indicated that the presence of commensals was necessary for Nod2 to localize to DCVs in Paneth cells. We next

© 2015 Nature America, Inc. All rights reserved.

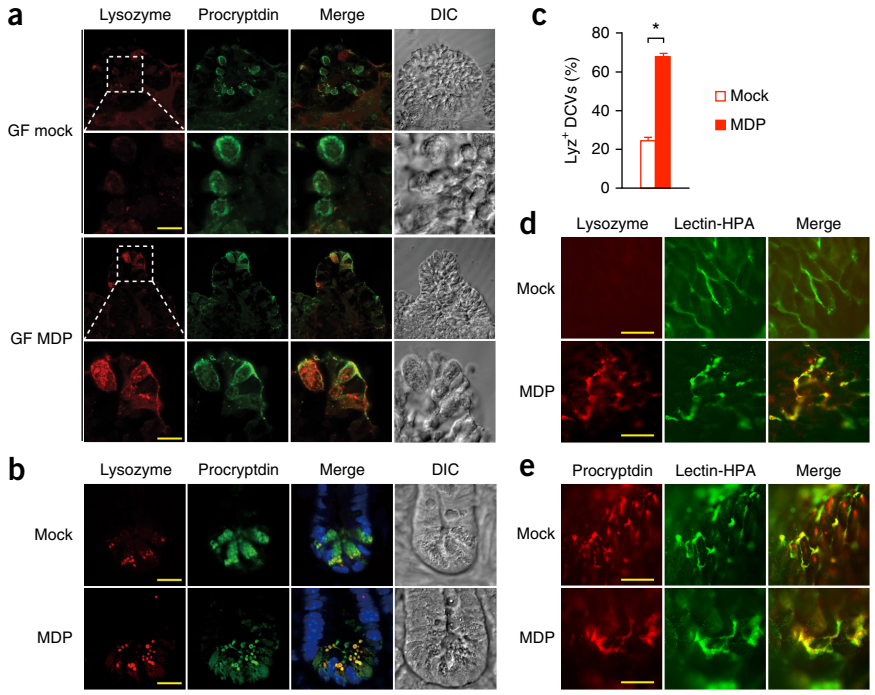

Figure 7 MDP restores lysozyme sorting in GF mice. (**a**) Confocal images of lysozyme and procryptdin in cultured crypt cells from GF mice treated with 2 μg ml^{-1} MDP or mock treated for 24 h. Scale bars, 10 μm. Boxed areas are shown at higher magnification in the panels below. (**b**) Confocal images of the indicated proteins in ileal crypts from GF mice treated with MDP (500 μg per mouse) or mock treated. Blue, counterstained nuclei. Scale bars, 10 μm. (**c**) Percentage of lysozyme-positive DCVs. DCVs from 30 Paneth cells per mouse were quantified in three mice for each treatment. Data are expressed as mean and s.e.m. *$P < 0.01$ (Student's *t*-test). (**d**,**e**) Whole-mount images of tissues taken from immediately above the ileal mucosal surface in mock- and MDP-treated GF mice and stained with lectin-HPA and anti-lysozyme (**d**) or anti-procryptdin (**e**). Scale bars, 20 μm. Data are representative of three independent experiments.

examined the localization of LRRK2 and Rab2a in *Nod2*$^{-/-}$ Paneth cells. Similar to our observations in Paneth cells from GF mice, the DCV localization of Rab2 and LRRK2 in *Nod2*$^{-/-}$ Paneth cells was greatly reduced compared with that in wild-type Paneth cells (**Fig. 6f–h**). Coimmunoprecipitation revealed interaction between LRRK2 and Nod2 when overexpressed in HEK293T cells and between the endogenous proteins in isolated crypts (**Fig. 6i–k**). Thus, Nod2 on DCVs might physically recruit LRRK2 for lysozyme sorting. These results indicate that Nod2 mediates the microbial signal to direct cargo sorting in DCVs.

Bacterial ligands restore lysozyme sorting

Next we asked whether binding of Nod2 by its ligands is sufficient for lysozyme sorting in Paneth cells from GF mice. We first treated cultured organoids derived from GF mice with the Nod2 cognate ligand MDP, a bacterial cell wall peptidoglycan. This treatment restored lysozyme staining in GF-derived Paneth cells in cultured organoids (**Fig. 7a**). Treatment of GF mice with MDP via oral gavage restored lysozyme staining in mature DCVs in Paneth cells compared with DCVs from mock-treated GF mice (**Fig. 7b**,**c**). This treatment also restored lysozyme in the intestinal lumens of GF mice in comparison with those of mock-treated GF mice, as detected by whole-mount staining against lysozyme (**Fig. 7d**), whereas procryptdin was unaffected (**Fig. 7e**). To determine whether other bacterial ligands might also restore lysozyme in GF mice, we treated cultured organoids derived from GF mice with a range of Nod1 and TLR agonists. In addition to MDP, lipopolysaccharide (LPS) treatment also restored lysozyme *in vitro* and *in vivo* (**Supplementary Fig. 7a–c**). Lysozyme staining was similar between wild-type and *Tlr4*$^{-/-}$ crypts, used as a control (**Supplementary Fig. 7d**), which suggested that TLR4 signaling is not involved in lysozyme sorting. In contrast, LPS treatment in GF mice restored the DCV localization of LRRK2 and Rab2a, but not Nod2 (**Supplementary Fig. 7e–g**), which indicated that LPS may engage in crosstalk with LRRK2 and Rab2a through some unknown mechanism(s). Thus, specific commensal bacterial ligands are sufficient for directing lysozyme sorting in Paneth cells in germ-free conditions. Our genetic and functional analyses demonstrate that symbiotic bacteria direct lysozyme sorting in Paneth cells through a molecular pathway including Nod2, LRRK2 and Rab2a (**Supplementary Fig. 8**).

DISCUSSION

Here we have described a specific lysozyme defect in *Lrrk2*$^{-/-}$ Paneth cells and used small intestinal crypt organoid cultures to investigate the molecular basis of this defect. Biochemical analysis showed that *Lrrk2*$^{-/-}$ Paneth cells lacked lysozyme because of a post-translational defect. Yeast two-hybrid screening identified Rab2a, which regulates DCV cargo trafficking in *C. elegans*[25], as a binding partner of LRRK2. Knockdown in crypt organoids indicated that Rab2a was required for lysozyme sorting in Paneth cells. Thus, our study describes a conserved Rab2a-dependent sorting-by-retention mechanism in mammalian cells and suggests that LRRK2 is required for the DCV localization of Rab2a in Paneth cells.

The presence of commensal microbes was required for lysozyme sorting promoting the DCV localization of Nod2. Consistent with this, bacterial ligands restored lysozyme sorting in Paneth cells in GF mice. It was previously reported that commensals promote DCV secretion[26]. Notably, in DCV-mediated exocytosis, selective cargo sorting occurs at a stage that precedes the final secretion step. Thus, two different steps, selective cargo sorting and final secretion, are separately regulated by commensals.

Our study shows that Nod2 and LRRK2 regulated the selective sorting of lysozyme, but not other proteins such as Reg3γ and procryptdin, by recruiting Rab2a onto the DCV surface. How Rab2a controls such selective sorting remains to be explored. In fact, little is known about how specific DCV protein cargos are successfully sorted inside DCVs while others are directed to the endosomal-lysosomal route during DCV maturation. Cargo receptors or chaperones may exist either in the lumen or on the DCV surface[29]. Members of the Rab family of small GTPase proteins are regulators of intracellular vesicle trafficking and have a key role in controlling the cellular fate of membrane receptors[36,37]. Therefore, a possible scenario is that Rab2a controls the cellular fate of certain cargo receptors on DCVs. Loss of Rab2a may cause the receptors, and consequently lysozyme, to be sent to lysosomes for degradation. Other cargos, such as Reg3γ and procryptdin, may have different receptors and therefore be unaffected by the loss of Rab2a from the surface of DCVs.

© 2015 Nature America, Inc. All rights reserved.

At the junction of commensals and mucosal immunity, Paneth cells have a key role in intestinal homeostasis. Abnormalities in vesicle trafficking in Paneth cells, characterized by diminished amounts of lysozyme-positive DCVs, have been noted in people with Crohn's disease[24,38]. Notably, in Paneth cells with defects in autophagy genes, intracellular vesicle trafficking is impaired, as shown by a diffuse lysozyme staining pattern and decreased secretion of lysozyme[24,39]. Such defects are dependent on persistent intestinal infection with murine norovirus[40]. The defects we observed in Paneth cells from *Nod2*$^{-/-}$, *Lrrk2*$^{-/-}$ and GF mice were different. First, the defects did not depend on norovirus infection, which was constantly monitored in our animal facility. Second, instead of displaying a diffuse staining pattern in autophagy-gene-defective Paneth cells, the lysozyme content was selectively and progressively diminished in more mature apical DCVs in Paneth cells from *Nod2*$^{-/-}$, *Lrrk2*$^{-/-}$ and GF mice, which indicated a cargo-sorting defect during DCV maturation. Despite these minor differences in mechanism, studies by us and others clearly highlight the role of dysregulated membrane trafficking in Paneth cells in IBD pathogenesis.

In our study, MDP and LPS, but not other tested agonists, promoted lysozyme sorting in GF mice, which suggests a relatively specific requirement for bacterial ligands in the lysozyme-sorting process. Other factors, such as autophagy, may also affect lysozyme sorting, but this remains to be explored. LRRK2 is involved in the endosomal-autophagic pathway[41], and Nod2, IRGM and ATG16L1 form a protein complex to modulate autophagosome formation[42–44]. Autophagy is not required for lysozyme trafficking under steady-state conditions[40]. However, whether autophagy regulates lysozyme sorting under stress conditions, such as infection or starvation, remains to be determined. It will be interesting to determine whether other factors, such as autophagy, crosstalk with Nod2 and LRRK2 to modulate lysozyme sorting.

Our data showed that LRRK2 participates in cargo sorting by recruiting Rab2a onto DCVs. A few members of the Rab small GTPase family have been found to associate with LRRK2, including Rab5b, Rab7L1 and Rab32 (refs. 45–47). Therefore, it is likely that LRRK2 regulates intracellular membrane trafficking in a cell-context-dependent manner. DCVs in neurons are responsible for the storage and secretion of important neurotropic factors. As a step toward clarifying the genetic involvement of *LRRK2* in Parkinson's disease, it would be worthwhile to examine whether LRRK2 similarly regulates Rab2a in neurons.

In summary, our study unravels a new mechanism by which symbiotic bacteria direct a cargo-sorting event to promote host defense against pathogens. Our study also provides an example of how molecular studies on IBD-susceptibility genes can provide insights into the complex nature of the reciprocal regulation between host and microbial organisms.

METHODS

Methods and any associated references are available in the online version of the paper.

Note: Any Supplementary Information and Source Data files are available in the online version of the paper.

ACKNOWLEDGMENTS

The authors thank M. Cookson (National Institutes of Health, Bethesda, Maryland, USA) for the LRRK2 expression vector, T. Kufer (Universität Hohenheim, Stuttgart, Germany) for the Nod2 expression vector, H. Tang (Chinese Academy of Sciences, Beijing, China) for *L. monocytogenes* strain 10403s, and Z. Chang (Tsinghua University, Beijing, China) for yeast two-hybrid screening reagents. The authors thank H. Zhang (Institute of Biophysics, Chinese Academy of Sciences, Beijing, China) for helpful discussions. This work was supported by the National Natural Science Foundation of China (31271521, 31422019, 81370906), the National Basic Research Program of China (2013CB531405, 2013CB531406), the Thousand Young Talents Program of China, and the Chinese Academy of Sciences–Novo Nordisk Foundation (NNCASGWP-2012-2). Z.Q. was supported by National Science Foundation of China (81101923) and the Beijing Natural Science Foundation (13G20203).

AUTHOR CONTRIBUTIONS

Q.Z. and Y.P. were responsible for the execution of experiments and data analysis. Y.P. and R.Y. were responsible for organoid culture. H. Wang and X.Z. were responsible for imaging analysis. B.Z., W.L. and H. Wei were responsible for the germ-free facility. Z.L. and Q.Z. wrote the manuscript with input from other authors. Z.L. supervised the study.

COMPETING FINANCIAL INTERESTS

The authors declare no competing financial interests.

Reprints and permissions information is available online at http://www.nature.com/reprints/index.html.

1. Cash, H.L., Whitham, C.V., Behrendt, C.L. & Hooper, L.V. Symbiotic bacteria direct expression of an intestinal bactericidal lectin. *Science* **313**, 1126–1130 (2006).
2. Alenghat, T. & Artis, D. Epigenomic regulation of host-microbiota interactions. *Trends Immunol.* **35**, 518–525 (2014).
3. Furusawa, Y., Obata, Y. & Hase, K. Commensal microbiota regulates T cell fate decision in the gut. *Semin. Immunopathol.* **37**, 17–25 (2015).
4. Hugot, J.P. *et al.* Association of NOD2 leucine-rich repeat variants with susceptibility to Crohn's disease. *Nature* **411**, 599–603 (2001).
5. Ogura, Y. *et al.* A frameshift mutation in NOD2 associated with susceptibility to Crohn's disease. *Nature* **411**, 603–606 (2001).
6. Kobayashi, K.S. *et al.* Nod2-dependent regulation of innate and adaptive immunity in the intestinal tract. *Science* **307**, 731–734 (2005).
7. Ramanan, D., Tang, M.S., Bowcutt, R., Loke, P. & Cadwell, K. Bacterial sensor Nod2 prevents inflammation of the small intestine by restricting the expansion of the commensal Bacteroides vulgatus. *Immunity* **41**, 311–324 (2014).
8. Petnicki-Ocwieja, T. *et al.* Nod2 is required for the regulation of commensal microbiota in the intestine. *Proc. Natl. Acad. Sci. USA* **106**, 15813–15818 (2009).
9. Barrett, J.C. *et al.* Genome-wide association defines more than 30 distinct susceptibility loci for Crohn's disease. *Nat. Genet.* **40**, 955–962 (2008).
10. Franke, A. *et al.* Genome-wide meta-analysis increases to 71 the number of confirmed Crohn's disease susceptibility loci. *Nat. Genet.* **42**, 1118–1125 (2010).
11. Anderson, C.A. *et al.* Meta-analysis identifies 29 additional ulcerative colitis risk loci, increasing the number of confirmed associations to 47. *Nat. Genet.* **43**, 246–252 (2011).
12. Zimprich, A. *et al.* Mutations in LRRK2 cause autosomal-dominant parkinsonism with pleomorphic pathology. *Neuron* **44**, 601–607 (2004).
13. Paisán-Ruíz, C. *et al.* Cloning of the gene containing mutations that cause PARK8-linked Parkinson's disease. *Neuron* **44**, 595–600 (2004).
14. Liu, Z. *et al.* The kinase LRRK2 is a regulator of the transcription factor NFAT that modulates the severity of inflammatory bowel disease. *Nat. Immunol.* **12**, 1063–1070 (2011).
15. Gardet, A. *et al.* LRRK2 is involved in the IFN-γ response and host response to pathogens. *J. Immunol.* **185**, 5577–5585 (2010).
16. Clevers, H.C. & Bevins, C.L. Paneth cells: maestros of the small intestinal crypts. *Annu. Rev. Physiol.* **75**, 289–311 (2013).
17. Vaishnava, S., Behrendt, C.L., Ismail, A.S., Eckmann, L. & Hooper, L.V. Paneth cells directly sense gut commensals and maintain homeostasis at the intestinal host-microbial interface. *Proc. Natl. Acad. Sci. USA* **105**, 20858–20863 (2008).
18. Adolph, T.E. *et al.* Paneth cells as a site of origin for intestinal inflammation. *Nature* **503**, 272–276 (2013).
19. Wilson, C.L. *et al.* Regulation of intestinal α-defensin activation by the metalloproteinase matrilysin in innate host defense. *Science* **286**, 113–117 (1999).
20. Kaser, A. *et al.* XBP1 links ER stress to intestinal inflammation and confers genetic risk for human inflammatory bowel disease. *Cell* **134**, 743–756 (2008).
21. Salzman, N.H., Ghosh, D., Huttner, K.M., Paterson, Y. & Bevins, C.L. Protection against enteric salmonellosis in transgenic mice expressing a human intestinal defensin. *Nature* **422**, 522–526 (2003).
22. Brandl, K., Plitas, G., Schnabl, B., DeMatteo, R.P. & Pamer, E.G. MyD88-mediated signals induce the bactericidal lectin RegIIIγ and protect mice against intestinal Listeria monocytogenes infection. *J. Exp. Med.* **204**, 1891–1900 (2007).
23. Chu, H. *et al.* Human α-defensin 6 promotes mucosal innate immunity through self-assembled peptide nanonets. *Science* **337**, 477–481 (2012).
24. Cadwell, K. *et al.* A key role for autophagy and the autophagy gene Atg16l1 in mouse and human intestinal Paneth cells. *Nature* **456**, 259–263 (2008).
25. Sumakovic, M. *et al.* UNC-108/RAB-2 and its effector RIC-19 are involved in dense core vesicle maturation in *Caenorhabditis elegans*. *J. Cell Biol.* **186**, 897–914 (2009).

© 2015 Nature America, Inc. All rights reserved.

26. Ayabe, T. *et al.* Secretion of microbicidal α-defensins by intestinal Paneth cells in response to bacteria. *Nat. Immunol.* **1**, 113–118 (2000).
27. Sato, T. *et al.* Single Lgr5 stem cells build crypt-villus structures *in vitro* without a mesenchymal niche. *Nature* **459**, 262–265 (2009).
28. Bowman, G.R., Cowan, A.T. & Turkewitz, A.P. *Biogenesis of Dense-core Secretory Granules* (Landes Bioscience and Springer Science + Business Media, 2009).
29. Kim, T., Gondre-Lewis, M.C., Arnaoutova, I. & Loh, Y.P. Dense-core secretory granule biogenesis. *Physiology (Bethesda)* **21**, 124–133 (2006).
30. Edwards, S.L. *et al.* Impaired dense core vesicle maturation in *Caenorhabditis elegans* mutants lacking Rab2. *J. Cell Biol.* **186**, 881–895 (2009).
31. Sasidharan, N. *et al.* RAB-5 and RAB-10 cooperate to regulate neuropeptide release in *Caenorhabditis elegans*. *Proc. Natl. Acad. Sci. USA* **109**, 18944–18949 (2012).
32. Satoh, Y., Ishikawa, K., Ono, K. & Vollrath, L. Quantitative light microscopic observations on Paneth cells of germ-free and ex-germ-free Wistar rats. *Digestion* **34**, 115–121 (1986).
33. Nieuwenhuis, E.E. *et al.* Cd1d-dependent regulation of bacterial colonization in the intestine of mice. *J. Clin. Invest.* **119**, 1241–1250 (2009).
34. Shanahan, M.T. *et al.* Mouse Paneth cell antimicrobial function is independent of Nod2. *Gut* **63**, 903–910 (2014).
35. Ogura, Y. *et al.* Expression of NOD2 in Paneth cells: a possible link to Crohn's ileitis. *Gut* **52**, 1591–1597 (2003).
36. Barr, F.A. Review series: Rab GTPases and membrane identity: causal or inconsequential? *J. Cell Biol.* **202**, 191–199 (2013).
37. Aloisi, A.L. & Bucci, C. Rab GTPases-cargo direct interactions: fine modulators of intracellular trafficking. *Histol. Histopathol.* **28**, 839–849 (2013).
38. VanDussen, K.L. *et al.* Genetic variants synthesize to produce Paneth cell phenotypes that define subtypes of Crohn's disease. *Gastroenterology* **146**, 200–209 (2014).
39. Cadwell, K., Patel, K.K., Komatsu, M. & Virgin, H.W. 4th & Stappenbeck, T.S. A common role for Atg16L1, Atg5 and Atg7 in small intestinal Paneth cells and Crohn disease. *Autophagy* **5**, 250–252 (2009).
40. Cadwell, K. *et al.* Virus-plus-susceptibility gene interaction determines Crohn's disease gene Atg16L1 phenotypes in intestine. *Cell* **141**, 1135–1145 (2010).
41. Alegre-Abarrategui, J. *et al.* LRRK2 regulates autophagic activity and localizes to specific membrane microdomains in a novel human genomic reporter cellular model. *Hum. Mol. Genet.* **18**, 4022–4034 (2009).
42. Travassos, L.H. *et al.* Nod1 and Nod2 direct autophagy by recruiting ATG16L1 to the plasma membrane at the site of bacterial entry. *Nat. Immunol.* **11**, 55–62 (2010).
43. Chauhan, S., Mandell, M.A. & Deretic, V. IRGM governs the core autophagy machinery to conduct antimicrobial defense. *Mol. Cell* **58**, 507–521 (2015).
44. Cooney, R. *et al.* NOD2 stimulation induces autophagy in dendritic cells influencing bacterial handling and antigen presentation. *Nat. Med.* **16**, 90–97 (2010).
45. MacLeod, D.A. *et al.* RAB7L1 interacts with LRRK2 to modify intraneuronal protein sorting and Parkinson's disease risk. *Neuron* **77**, 425–439 (2013).
46. Yun, H.J. *et al.* An early endosome regulator, Rab5b, is an LRRK2 kinase substrate. *J. Biochem.* **157**, 485–495 (2015).
47. Waschbüsch, D. *et al.* LRRK2 transport is regulated by its novel interacting partner Rab32. *PLoS ONE* **9**, e111632 (2014).

© 2015 Nature America, Inc. All rights reserved.

ONLINE METHODS

Statistical analysis. Statistical analyses were done with assistance from GraphPad Prism software. The results are expressed as the mean and s.e.m. unless otherwise indicated.

Mice. *Lrrk2*$^{-/-}$ and *Myd88*$^{-/-}$ mice on a C57BL/6J background were from Jax. *Nod2*$^{-/-}$ mice (RIKEN), which have been described previously[48], were originally on a C57BL/6J congenic background and were backcrossed with wild-type C57BL/6J mice for two more generations after arriving in our facility. All SPF mice, including wild-type C57BL/J6, were bred and housed in a barrier facility accredited by the Association for Assessment and Accreditation of Laboratory Animal Care International for SPF mice (Laboratory Animal Facility of Tsinghua University). The facility was routinely checked for the absence of specific infectious agents, including murine novovirus and *Helicobacter*. All procedures were done with the approval of the Animal Ethics Committee of Tsinghua University.

GF C57BL/6J mice were maintained in GF conditions in vinyl isolators in the animal facility in Third Military Medical University and were used according to protocols approved by the Institutional Animal Care and Use Committee of Third Military Medical University. Mice were euthanized immediately after being taken out of the isolators.

Cell culture and reagents. HEK293T cells (CRL-3216, ATCC) were verified with tests recommended by ATCC, including a morphology check by microscopy and growth curve analysis. The cells were tested for mycoplasma contamination by Hoechst 33258 staining as recommended by ATCC and were found to be free of contamination. The cells were cultured in DMEM (Invitrogen) supplemented with 10% FBS (Hyclone) and 1% Pen-Strep (Invitrogen) in a 5% CO_2 atmosphere. All chemical reagents were from Sigma-Aldrich unless otherwise mentioned. Ultrapure LPS, Pam3CSK4, iE-DAP, and poly(dA:dT) were from Invivogen.

Antibodies. The following primary antibodies were used: anti-LRRK2 (Epitomics, MJFF2 c41-2), anti-lysozyme (Abcam, ab36362), anti-Rab2a (Santa Cruz Biotechnology, SC-28567), anti-Rab10 (Santa Cruz Biotechnology, SC-6564), anti-Reg3γ (Abgent, AP5606c), anti-Myc (Roche, clone 9E10, 11667149001), anti-GFP (Roche, 11814460001), anti-Nod2 (H-300; Santa Cruz Biotechnology, SC-30199), and anti-actin (Sigma, AC15, A5441). A rabbit antibody to procryptdin was generated as described[49]. The prosegment (DPIQNTDEET KTEEQPGEDD QAVSVSFGDP EGTSLQEES), which is conserved in all mouse procryptdin, was conjugated to KLH and used to immunize rabbits in complete Freund's adjuvant. Immunization was boosted twice, and the antiserum titer was evaluated by an enzyme-linked immunosorbent assay. Anti-procryptdin was further purified on a Protein A–agarose column (Sigma). Some of the rabbit anti-procryptdin was further conjugated with Alexa Fluor 555 with a conjugation kit (Invitrogen, A20187) according to the manufacturer's recommended protocol. Fluorophore-conjugated secondary antibodies were all from Invitrogen.

Plasmids. pCMV-2xMyc-LRRK2 was a kind gift from Dr. M. Cookson (National Institutes of Health). The human *Nod2* cDNA was cloned into the pEGFP vector from a human Nod2-expressing plasmid that was a kind gift from Dr. T. Kufer (Universität Hohenheim). Human and mouse *Rab2a* cDNA were reverse-transcribed from mRNA prepared from HEK293T cells and mouse brain, respectively, and cloned into the pEGFP vector. Sequences were confirmed by Sanger sequencing.

Bacterial infection. Sex- and age-matched (6–8 weeks old) wild-type and *Lrrk2*$^{-/-}$ littermates were used for all the infection experiments, which were performed under BL2 conditions. Sex- and age-matched (6–8 weeks old) wild-type and *Nod2*$^{-/-}$ mice were housed together 2 weeks before infection. For intestinal infection experiments, mice were infected by gastric gavage with 10^9 *L. monocytogenes* strain 10403s per mouse. Bacterial burden, measured in CFU, was assayed as described[20]. Feces were collected under sterile conditions 10 h after infection, and bacterial burden was determined as CFU per gram dry weight. Spleen and liver tissues were collected under sterile conditions after mice were euthanized 72 h after infection, and bacterial burden was determined as CFU per organ. For systemic infection, mice were infected with 10^4 *L. monocytogenes* per mouse by intravenous tail vein injection. Mice were euthanized 24 h and 48 h after infection. Bacterial burden in spleen and liver tissues was measured as described above.

Recombinant lysozyme supplementation. Sex- and age-matched (6–8 weeks old) wild-type and *Lrrk2*$^{-/-}$ littermates received 100 mg/kg recombinant lysozyme (Sigma, L1667) or PBS by gastric gavage every 24 h for 7 consecutive days. 24 h after the final treatment, mice were infected with 10^9 *L. monocytogenes* by gastric gavage. Bacterial burden was measured as described above.

Microbiota DNA extraction and analysis. DNA from intestinal microbiota was isolated with the Qiagen stool isolation kit according to the manufacturer's instructions. DNA concentration was measured by NanoDrop, and molecular size was estimated by agarose gel electrophoresis. Universal primers 338F and 806R were used for PCR amplification of the V3–V4 hypervariable regions of 16S rRNA genes (338F, 5′-ACTCCTACGGGAGGCAGCA-3′; 806R, 5′-GGACTACHVGGGTWTCTAAT-3′) and contained Illumina 3′ adaptor sequences as well as a 12-bp barcode. Sequencing was done on an Illumina MiSeq PE300. A total of 504,002 sequences were included in the study. The average number of sequences per specimen was 31,500, with a minimum of 22,773 and a maximum of 39,647. The average sequence length was 432 bases. Raw sequencing reads were de-noised, filtered according to barcode and primer sequences, and classified with Mothur. Chimeric sequences identified by Mothur and nonreplicated sequences were removed. The high-quality reads were clustered into operational taxonomic units (OTUs) by Mothur. The OTUs that reached a nucleotide-similarity level of 97% were used for alpha diversity (Shannon), richness (ACE and Chao1), Good's coverage, and rarefaction curve analysis with Mothur. Phylogenetic beta diversity measures such as unweighted UniFrac distance metrics analysis and principal-component analysis were done with OTUs for each sample with the Mothur program.

For taxonomy-based analyses, we determined a representative sequence for each OTU by selecting the most abundant sequences in that OTU. These representative sequences were classified and assigned to a taxonomic string with the Ribosomal Database Project Classifier.

Fecal microbiota transplantation. For bacterial-transplantation experiments, fecal microbiota from wild-type or *Lrrk2*$^{-/-}$ mice housed in separate cages were administered to 8-week-old GF wild-type mice by gastric gavage. Recipient mice were housed in separate isolators and euthanized or orally infected with *Listeria* as described above at day 14 after transplantation. Cecum contents from the conventionalized GF mice were collected for microbiota analysis to confirm the bacterial colonization.

***In vivo* MDP and LPS treatment in GF mice.** GF mice in vinyl isolators received MDP (500 μg/mouse) in 100 μl endotoxin-free PBS, LPS (500 μg/mouse) in 100 μl endotoxin-free PBS, or PBS (mock treatment) twice by mouth, with treatments 12 h apart. Four hours after the second treatment, mice were killed and intestinal tissues were processed as described above.

Intestinal organoid culture. Intestinal organoids were cultured according to a published method, with minor changes in crypt isolation[27,50]. After fat and connective tissues had been removed, a 5-cm-long section of distal ileum was opened longitudinally and rinsed with cold PBS. The tissue was then washed vigorously in 20 ml cold PBS in a 50-ml tube for 1 min and rinsed again in cold PBS. The tissue was then chopped into pieces smaller than 3–4 mm^2 and incubated at 37 °C for 20 min with 2 ml 0.1% collagenase solution. Tissue sections were pipetted up and down every 7 min during the incubation. Tissue sections were then transferred to another 2 ml of fresh collagenase solution for 20 min, during which the digestion reaction was pipetted up and down every 7 min and monitored for the release of crypts. Digestion was stopped by dilution with 20 ml cold PBS when around 70% of the crypts had been released, and the digests were filtered through a 70-μm cell strainer. The released crypts were pelleted by centrifugation at 100*g* for 5 min. Pelleted crypts (~500) were then mixed with 50 μl Matrigel (Invitrogen) and plated on glass coverslips (10 mm in diameter) in 24-well plates. After Matrigel polymerization, 500 μl growth medium was added to each well.

© 2015 Nature America, Inc. All rights reserved.

Growth medium was changed every 3 or 4 d. Every week, organoids were retrieved from the Matrigel, mechanically dissociated, and plated into fresh Matrigel. Culture medium contained Advanced DMEM/F12 (Invitrogen) supplemented with L-glutamine (Invitrogen), 1% Pen-Strep (Invitrogen), 10 μM Hepes (Invitrogen), N2 supplement 1:100 (Invitrogen), B27 supplement 1:50 (Invitrogen), 50 ng/ml epidermal growth factor (Peprotech), 500 ng/ml R-spondin 1 (R&D Systems), 100 ng/ml Noggin (R&D Systems), and 10 ng/ml Wnt-3a (Peprotech).

Isolation of CD24$^+$ Paneth cells. Crypts from small intestine were isolated as described above. Isolated crypts were digested into single-cell suspension by 30 min of incubation at 37 °C in TrypLE Express supplemented with 2,000 U/ml DNase I. Single cells were incubated on ice for 30 min with PerCP-Cy5.5–conjugated anti-CD24 (Ebiosciences, 45-0242-80) in PBS with 2% FBS, washed three times with PBS with 2% FBS, and subsequently sorted on an AriaIII. Both CD24$^-$ and CD24$^+$ cells were collected and used for immunoblotting analysis. Lysozyme staining was done after cells had been stained with CD24, fixed with 4% paraformaldehyde (PFA) for 10 min at 4 °C, and treated with 1× permeabilization buffer (Ebiosciences, 00-8333-56) for 10 min. Cells were then incubated with anti-lysozyme and subsequently with allophycocyanin-conjugated anti–mouse immunoglobulin G2a (Ebiosciences, 17-4210-80) and analyzed on a FACScalibur.

Treatment of cultured organoids. Freshly plated organoids were treated with leupeptin (100 μM), Brefeldin A (1 μg/ml), MDP (2 μg/ml), LPS (2 μg/ml), Pam3CSK4 (2 μg/ml), iE-DAP (10 μg/ml), dA:dT (10 μg/ml), polyI:C (10 μg/ml) and flagellin (10 μg/ml) or mock-treated for 24 h in culture medium before being washed, fixed with 4% PFA in PBS, and processed for immunostaining or collected for immunoblotting analysis.

siRNA transfection of cultured organoids. Cultured organoids (~1,000) were manually disrupted by vigorous pipetting in PBS. Cells were pelleted by centrifugation at 200*g* for 5 min, and PBS was removed. Pelleted cells were suspended in 100 μl premade transfection mixture at 37 °C for 20 min, after which cells were pelleted, suspended, and plated in Matrigel with culture medium as described above. Cells were collected for immunoblotting analysis or fixed for immunostaining analysis 72 h after transfection. When applicable, cells were treated with leupeptin or DMSO 48 h after transfection. Leupeptin treatment was conducted as described above.

We prepared the transfection mixture by mixing 50 μl Opti-MEM containing 200 nM siRNA oligos and 50 μl Opti-MEM mixed with 3 μl X-TremeGENE transfection reagent (Roche), which was incubated at room temperature for 20 min. Control and Rab2a siRNA oligos were from Invitrogen (*Silencer* Select). The Rab2a oligos had the following sense sequences: (1) CAUGCUUAUUGGAAAUAAAtt, (2) GGAGAGAAGUGAAAAAGGAtt. The Rab27a oligo had the following sense sequence: UCGACCUGACAA AUGAGCAAAGUUU. The Nod2 oligo had the following sense sequence: CGCACAGAGUUGCAACUGAtt.

Crypt lysate and supernatant preparation and *in vitro* bacterial-killing assay. Crypts were isolated as described above. *In vitro* bacterial killing was conducted as previously described, with minor changes[26]. We resuspended 2,000 isolated crypts in 2 ml DMEM with 1 μg/ml LPS (from *Escherichia coli* 0111:B4) and incubated them at 37 °C for 30 min. Supernatants were collected after centrifugation at 500*g* for 10 min. We measured bactericidal activity by incubating 300 μl supernatant at 37 °C with 33 μl DMEM containing 3.3×10^7 CFU *L. monocytogenes* with shaking at 70 rpm for 1 h. Another 200 μl supernatant was precipitated with trichloroacetic acid (TCA). To prepare crypt lysates, we pelleted 2,000 crypts and lysed them in 1 ml lysis buffer (50 mM Tris-HCl, 150 mM NaCl, 2 mM EDTA, 0.1% SDS, 1% NP-40, protease inhibitor cocktail) by incubation on ice for 30 min before centrifuging them at 10,000*g* for 10 min. Supernatants were collected as crypt lysates. Lysozyme levels were analyzed by immunoblotting of lysates and TCA-precipitated supernatant fractions. Levels of Reg3γ and actin were analyzed as loading controls.

Immunofluorescence staining of tissue sections. Mouse tissues were fixed in 4% PFA-PBS overnight, dehydrated and embedded in paraffin. Tissue slices (6 μm in thickness) were mounted on positively charged glass and dewaxed. Antigen retrieval was achieved by incubation in 0.01 M sodium citrate buffer (pH 6.0) for 25 min in a boiling steamer. Slides were then blocked with PBS supplemented with normal goat serum blocking reagent (Wuhan Boster, China) for 30 min and subjected to sequential incubation with primary antibodies at 4 °C overnight and fluorophore-conjugated secondary antibodies at room temperature for 2 h. When applicable, slides were further incubated with fluorophore-conjugated anti-procryptdin at 4 °C overnight. Between each incubation step, slides were washed with PBS three times for 5 min. 10% goat serum was present throughout all antibody incubation steps. Slides were then counterstained with ToPro3 and mounted in Fluoromount-G (SouthernBiotech). Confocal images were obtained with an Olympus TM FluoView 1200 or Zeiss LSM 710 imaging system under a 63× oil-immersion objective. For direct comparisons between wild-type and different knockout mice or between mock-treated and treated mice, we performed the whole procedure side by side for the relevant mice from the point of tissue harvesting.

Image-based quantification of positively stained DCVs. Quantification of DCVs was done by a blinded investigator. DCVs in 30 Paneth cells from each animal were quantified for positive staining for the specified proteins. Data were averaged and plotted with GraphPad Prism software. The RGB tool in Image J was used for categorization of lysozyme-containing DCVs in GF and SPF mice.

Immunofluorescence staining of cultured organoids. Organoids grown on glass coverslips were washed once with ice-cold PBS and fixed with ice-cold 4% PFA in PBS for 15 min. Organoids on coverslips were then washed three times with PBS and blocked with antibody dilution buffer (PBS supplemented with 10% goat serum and 0.1% saponin) for 30 min. Organoids on coverslips were incubated with primary antibodies at 4 °C overnight and then with fluorophore-conjugated secondary antibodies at room temperature for 2 h. Samples were washed in PBS containing 0.1% Tween-20 three times for each step. Antibody dilution buffer was used throughout for antibody incubation steps. Coverslips were then counterstained and mounted on slides in Fluoromount-G (SouthernBiotech). Confocal images were obtained with a Zeiss LSM 710 imaging system under a 63× oil-immersion objective. For imaging comparisons between organoids that had undergone various treatments, samples were processed side by side for the whole procedure.

Whole-mount immunofluorescence staining. Ileal sections were opened longitudinally after the adipose tissues had been stripped off. Tissues were fixed in 4% PFA for 1 h before being rinsed three times for 5 min in PBS and incubated with primary antibodies for 2 h at room temperature. After PBS washes, tissues were incubated with Alexa Fluor–conjugated secondary antibodies and fluorescein isothiocyanate–labeled *H. pomatia* lectin (Invitrogen, L11271) for 2 h at room temperature. Tissues were mounted on glass slides and examined under a Nikon Eclipse 90i or Ti-s automated fluorescence microscope with a 10× objective.

Immunohistochemical staining of tissue sections. Tissue slices (6 μm in thickness) from PFA-fixed and paraffin-embedded tissue blocks were mounted on positively charged glass and dewaxed. We retrieved antigen by boiling the slides in 10 mM sodium citrate buffer (pH 6.0) for 25 min. The slides were washed with PBS, after which IHC was done with an UltraSensitive TM S-P Kit (Maixin Bio, China). The slides were first treated with hydrogen peroxide for 10 min to block endogenous peroxidase and then incubated with a blocking serum for 20 min at room temperature. The slides were then sequentially incubated with mouse anti-lysozyme overnight at 4 °C, biotinylated secondary goat anti-mouse for 20 min at room temperature, and streptavidin-peroxidase for another 20 min at room temperature. Between each incubation step, slides were washed with PBS three times for 5 min. Immunoreactivity was detected with diaminobenzidine. The slides were counterstained with hematoxylin, mounted, and observed with a light microscope (Nikon Eclipse 90i).

Electron microscopic analyses of DCVs in Paneth cells. Sections of distal ileum from euthanized mice were washed with cold PBS and cut into pieces 1–2 mm in length. Tissues were then fixed in 0.1 M sodium phosphate buffer

© 2015 Nature America, Inc. All rights reserved.

doi:10.1038/ni.3233

(pH 7.2) containing 2.5% glutaraldehyde and 2% paraformaldehyde at 4 °C overnight. Dehydration was done with an ethanol gradient followed by infiltration and embedment with an SPI-Pon 812 Epoxy Embedding Kit. Sections were cut on a Leica Ultracut Ultramicrotome (Leica EM UC6) and stained with uranyl acetate and lead citrate. The digital images were obtained under a transmission electron microscope (Hitichi H-7650) at 80 kV. Halo regions of DCVs were measured from a total of 500 DCVs from two animals for each genotype.

Isolation and quantification of mRNA from crypts. RNA was extracted from isolated crypts with TRIzol according to the manufacturer's instructions (Invitrogen). Reverse transcription was done with a PrimerScript RT reagent kit (Takara). Quantitative PCR reactions were then carried out with Light Cycler SYBR green DNA master mix (Takara) on an ABI7500 thermal cycler in triplicate. The following thermal cycling conditions were used: 50 °C for 2 min and 95 °C for 10 min, followed by 40 cycles of 95 °C for 15 s and 60 °C for 1 min. The specificity of quantitative PCR was verified with melting curves for each PCR reaction. Primers specific for mouse GAPDH were used as the control to normalize loading. The amount of target mRNA was determined by the difference in cycle threshold (C_t) values between the target and loading control. Primers for quantitative PCR were as follows:

Mouse Rab2a-F: TAGAGTTTGGTGCTCGGATG
Mouse Rab2a-R: CCGTGTGATAGAACGAAAGG
Mouse Nod2-F: GCCCTACAGCTGGATTACAAC
Mouse Nod2-R: CGCCTGTGATGTGATTGTTC
Mouse LRRK2-F: GCTATCTTGCATTTCGTTGTGC
Mouse LRRK2-R: CCCAGGATTCCCAATGAACC
Mouse Lysozyme1-F: GCCAAGGTCTACAATCGTTGTGAGTTG
Mouse Lysozyme1-R: CAGTCAGCCAGCTTGACACCACG
Mouse GAPDH-F: TGTTCCTACCCCCAATGTGT
Mouse GAPDH-R: GGTCCTCAGTGTAGCCCAAG

Yeast two-hybrid screening. Yeast two-hybrid screening was done according to the manufacturer's guidelines (Clontech). LRRK2 was cloned into pGBKT7 and transformed into yeast AH109. A mouse 7.5-d embryo library in pACT2 was screened for potential interacting partners in the yeast strain Y187. After the two yeast strains had been mated, zygotic cells were plated on quadruple dropout medium (QDO)–X-α-galactosidase to select for putative positive two-hybrid interactions for further analysis. The pACT2 AD plasmids of the selected colonies were recovered in *E. coli* and identified by sequencing. In order to confirm the protein-protein interactions of interest, we transformed the target plasmid combinations into yeast AH109 and confirmed on QDO–X-α-galactosidase plates.

Immunoprecipitation. 2×10^6 transfected HEK293T cells or 10^6 isolated crypts were collected, washed with 1 ml cold PBS, and lysed in 400 μl cold immunoprecipitation buffer (50 mM Tris, 150 mM NaCl, 2 mM EDTA, 1% NP-40, 0.5 mM PMSF, protease inhibitor cocktail from Roche) on ice for 30 min. Cell nuclei and debris were removed by centrifugation at 10,000*g* for 10 min at 4 °C. 10-μl samples of supernatants were saved for input. The rest of the supernatants were precleared with 15 μl protein G–conjugated DYNAbeads (Invitrogen) for 30 min at 4 °C. Immunoprecipitation antibody (1–2 μg) was added to supernatants for 2 h at 4 °C before 15 μl DYNAbeads were added to pull down protein-antibody complexes for 1 h. The antibody complex bound to DYNAbeads was washed three times with 400 μl immunoprecipitation buffer before being eluted with 30 μl SDS sample buffer (1×). Both inputs and eluents underwent immunoblotting analysis.

48. Zong, J. *et al.* NOD2 deletion promotes cardiac hypertrophy and fibrosis induced by pressure overload. *Lab. Invest.* **93**, 1128–1136 (2013).
49. Ayabe, T. *et al.* Activation of Paneth cell α-defensins in mouse small intestine. *J. Biol. Chem.* **277**, 5219–5228 (2002).
50. Miyoshi, H. & Stappenbeck, T.S. *In vitro* expansion and genetic modification of gastrointestinal stem cells in spheroid culture. *Nat. Protoc.* **8**, 2471–2482 (2013).

© 2015 Nature America, Inc. All rights reserved.